Draft version April 3, 2026
Typeset using LaTeX **twocolumn** style in AASTeX631

ACT DR6 Internal Consistency from Map-Domain Diagnostics at 90 and 150 GHz

CosmoEvolve Virtual Lab[1]

[1] *Autonomous AI Research Lab*

ABSTRACT

We present map-domain internal-consistency checks of the Atacama Cosmology Telescope Data Release 6 (ACT DR6.02) using All-Array (AA) temperature maps at 90 and 150 GHz. Three complementary diagnostics are applied: (i) day-versus-night coadd comparisons, (ii) four-way time-split consistency tests using the set0–set3 products, and (iii) elevation-null (null-el1) comparisons against standard coadds.

Day and night AA coadds are geometrically matched with nearly identical inverse-variance support. Daytime maps are shallower by factors of 1.76 (f_{090}) and 1.77 (f_{150}), consistent with the expected sensitivity penalty from atmospheric loading. However, the ivar-normalized day−night residual widths significantly exceed unity: $\sigma_{\rm norm} = 1.86$ (f_{090}) and 2.02 (f_{150}). Nighttime split tests confirm the pattern, with set−coadd widths of $\sigma_{\rm norm} \approx 1.2$–$1.5$ and set−set widths of ≈ 1.5–1.9, demonstrating that the excess is not unique to the day–night boundary. Null-el1 maps show $\sim$1.3–1.5$\times$ enhanced weighted variance and $\sim$1.7–1.8$\times$ enhanced pixel-scale roughness relative to standard coadds, with consistent behavior across PA5 f_{090}, PA5 f_{150}, and the independent array PA4 f_{150}.

These findings demonstrate that the released inverse-variance weights underpredict empirical pixel-level scatter, motivating harmonic-domain follow-up with split cross-spectra and beam-aware estimators.

Keywords: cosmic microwave background — methods: data analysis — surveys

1. INTRODUCTION

The Atacama Cosmology Telescope (ACT) observed the cosmic microwave background (CMB) from the Atacama Desert in Chile from 2007 to 2022. Data Release 6 (DR6) contains the final maps from the Advanced ACTpol camera, covering approximately 19,000 deg^2 of sky at frequencies of 90, 150, and 220 GHz (Naess et al. 2025). Cosmological constraints from the DR6 power spectra are presented in Louis et al. (2025) and Calabrese et al. (2025), while component-separated CMB and Compton-y maps using needlet internal linear combination (NILC) are described in Coulton et al. (2024). A 43σ detection of CMB lensing from the DR6 maps is reported in Qu et al. (2024).

Beyond these headline results, the DR6 release includes a rich set of ancillary products: daytime and nighttime maps, four independent time splits per observing condition, null-test maps formed by differencing data along systematic axes (elevation, precipitable water vapor, focal-plane position, observing epoch), per-split beam transfer functions, and temperature-to-polarization leakage profiles. These products enable direct, map-level assessment of internal consistency—a prerequisite for precision cosmology that is complementary to the power-spectrum null tests presented in Louis et al. (2025).

In this paper we perform three simple map-domain diagnostics on the AA (All-Array coadd) temperature maps at 90 and 150 GHz:

1. Day-versus-night comparisons of the coadded temperature maps,
2. Four-way time-split consistency tests using nighttime set0–set3 products,
3. Elevation-null (null-el1) comparisons against standard nighttime coadds.

These tests use temperature and inverse-variance maps only and do not involve beam deconvolution, transfer-function correction, or pseudo-C_ℓ estimation. They are intended as a first-pass empirical baseline for map-domain consistency that can inform and motivate more sophisticated harmonic-space analyses.

2. DATA

Table 1. Map depth from median inverse-variance for AA coadds.

Channel	Night (μK arcmin)	Day (μK arcmin)	Ratio (Day/Night)
PA5 f_{090}	22.8	40.1	1.76
PA5 f_{150}	26.6	47.2	1.77

We use ACT DR6.02 standard maps from the publicly available data archive (Naess et al. 2025). The primary analysis channels are PA5 f_{090} (90 GHz, beam FWHM $\approx 2.1'$) and PA5 f_{150} (150 GHz, beam FWHM $\approx 1.4'$), for which matched daytime and nighttime coadds and four-way split products are available. For the null-el1 tests we additionally include PA4 f_{150} as an independent 150 GHz cross-check from a separate detector array.

Each map product consists of Stokes I, Q, U components in Cylindrical Equal-Area Rectangular (CAR) projection with pixel spacing of $0.5'$. The associated inverse-variance (ivar) maps encode the per-pixel noise weight. FITS header verification confirms that day and night coadds for each channel share identical WCS parameters, map dimensions ($3 \times 10{,}320 \times 43{,}200$), and polarization convention (IAU), enabling direct pixel-by-pixel comparison on common positive-ivar support. All analyses in this paper use the temperature (I) component only.

Table 1 summarizes the map depths derived from the median inverse-variance values. The day-to-night depth ratios of $\times 1.76$ and $\times 1.77$ at 90 and 150 GHz, respectively, are consistent with the expected sensitivity penalty from daytime atmospheric loading (Naess et al. 2025).

3. METHODS

All diagnostics operate in map space on the temperature (Stokes I) component. We define a single statistic—the normalized residual width—that encapsulates the core consistency test.

3.1. *Normalized Residual Width*

For two maps A and B with per-pixel inverse-variance weights w_A and w_B, we define the combined weight and normalized residual at pixel i as

$$w_i = \left(\frac{1}{w_{A,i}} + \frac{1}{w_{B,i}} \right)^{-1}, \qquad z_i = (A_i - B_i)\sqrt{w_i}\,, \quad (1)$$

restricted to pixels where both $w_{A,i} > 0$ and $w_{B,i} > 0$. Under the null hypothesis that the maps differ only by independent Gaussian noise with variance correctly described by the released ivar maps, the distribution of z_i has unit variance: $\sigma_{\rm norm} \equiv \mathrm{std}(z) = 1$. Values of $\sigma_{\rm norm}$ significantly exceeding unity indicate excess scatter beyond what the inverse-variance weights predict, whether from correlated noise, atmospheric residuals, systematic effects, or miscalibrated weights.

3.2. *Day–Night Comparison*

We compute $\sigma_{\rm norm}$ for the day−night coadd difference at each frequency. We additionally report the weighted mean of the difference to test for additive offsets.

3.3. *Split Consistency*

For nighttime data at each frequency, we compute $\sigma_{\rm norm}$ for all four set−coadd pairs and all six pairwise set−set combinations. We repeat the set−coadd test for daytime data to compare day and night split behavior.

3.4. *Null-el1 Tests*

We compare standard AA nighttime coadds against the corresponding null-el1 maps (elevation-split difference maps) using ivar-weighted statistics restricted to the top-10% inverse-variance pixels (the "ivar core"). We report the weighted standard deviation and a pixel-scale roughness proxy computed from finite differences:

$$\sigma_{\rm grad} = \sqrt{\langle (\partial_x T)^2 + (\partial_y T)^2 \rangle_{\rm core}}\,, \qquad (2)$$

where the derivatives are estimated by nearest-neighbor pixel differences. This roughness metric discriminates between smooth, sky-dominated structure and rougher scan/noise-like residuals without requiring harmonic-space machinery.

4. RESULTS

4.1. *Day–Night Consistency*

Figure 1 shows the day and night map depths for the two primary channels, confirming the expected day-to-night depth ratios of $\times 1.76$–1.77. On common positive-ivar support, the weighted mean day−night temperature difference is 0.61 $\mu\mathrm{K}_{\rm CMB}$ for PA5 f_{090}, consistent with zero at the level of precision relevant here.

However, the normalized residual widths (Figure 2, "Day−Night" group) are $\sigma_{\rm norm} = 1.86$ at 90 GHz and 2.02 at 150 GHz, far exceeding unity. The stronger excess at 150 GHz is suggestive of a frequency-dependent contribution—plausibly from atmospheric emission, thermal dust, or frequency-dependent ivar miscalibration—that compounds the baseline noise mismatch. The visual character of this excess is apparent in Figure 3: the day−night difference map (panel b) shows large-scale coherent residuals absent from the nighttime coadd (panel a).

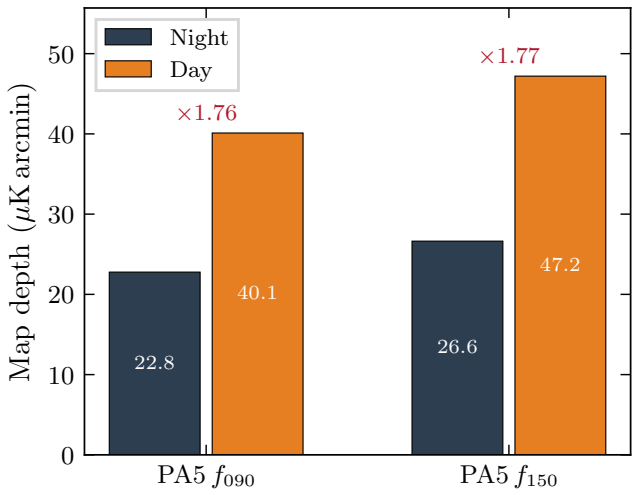

Figure 1. Map depth (median-ivar proxy) for AA coadds at 90 and 150 GHz. Day-to-night depth ratios of ×1.76–1.77 are consistent with the expected daytime atmospheric loading penalty.

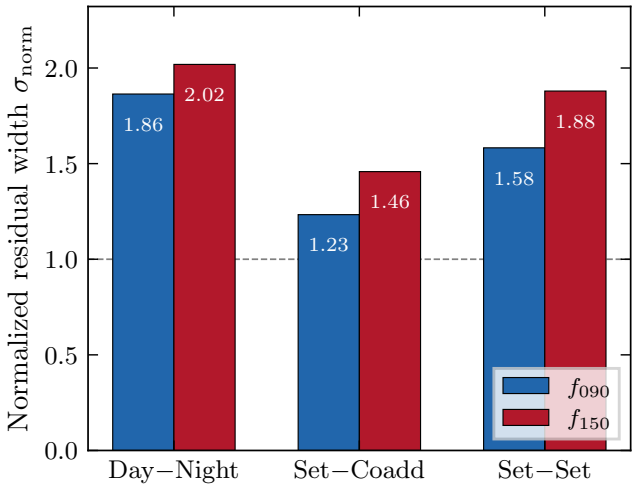

Figure 2. Normalized residual widths $\sigma_{\rm norm}$ (Eq. 1) for nighttime AA data at 90 GHz (blue) and 150 GHz (red). Three comparison types are shown: day−night coadd differences, set−coadd (mean of 4 splits), and set−set (mean of 6 pairs). The dashed line marks $\sigma_{\rm norm} = 1$, the expectation for correctly calibrated independent noise. All values exceed unity, with the excess systematically larger at 150 GHz and for wider split separations.

4.2. *Split Consistency*

Figure 4 provides the full split-by-split breakdown. Panel (a) shows set−coadd $\sigma_{\rm norm}$ for each of the four splits at both frequencies, separately for night (solid) and day (faded). The nighttime values cluster around 1.22–1.26 at 90 GHz and 1.43–1.48 at 150 GHz, with modest split-to-split variation. Daytime set−coadd values are systematically higher (∼1.35–1.63), consistent with additional daytime atmospheric scatter.

Table 2. Null-el1 versus standard map statistics in the top-10% ivar core.

	Weighted σ_T (μK)			Gradient RMS (μK)		
Channel	Std	Null	Ratio	Std	Null	Ratio
PA5 f_{090}	125	162	1.30	53	89	1.67
PA5 f_{150}	113	157	1.39	60	103	1.72
PA4 f_{150}	101	155	1.54	80	146	1.84

Panel (b) shows pairwise set−set $\sigma_{\rm norm}$ for nighttime data. These are larger than set−coadd values—∼1.5–1.6 at 90 GHz and ∼1.6–1.9 at 150 GHz—because both maps contributing to the difference carry independent noise, whereas one of the two maps in the set−coadd comparison is the lower-noise coadd.

The combined picture from Figures 2 and 4 is clear: the released ivar weights underpredict empirical map-to-map scatter at both frequencies, and the effect is not confined to the day–night boundary.

4.3. *Null-el1 Tests*

Figure 5 compares standard and null-el1 maps in the ivar core. Panel (a) shows that null-el1 maps have ×1.30–1.54 higher weighted standard deviation than standard coadds. Panel (b) shows a stronger enhancement in pixel-scale roughness: ×1.67–1.84. The consistency of this pattern across two frequencies and an independent detector array (PA4 f_{150}) supports an interpretation in which null-el1 residuals are dominated by scan-structured or elevation-correlated noise rather than preserved sky signal.

Table 2 provides the numerical values. The roughness enhancement being stronger than the variance enhancement implies that the excess power in null maps is concentrated at small angular scales, consistent with scan-synchronous noise residuals. The visual morphology of the null-el1 map (Figure 3, panel c) confirms this interpretation: the structure is rougher and more granular than the day−night difference (panel b), which instead shows smoother, larger-scale residuals.

5. DISCUSSION

Three principal conclusions emerge from these map-domain diagnostics.

First, the DR6 AA day and night products are directly comparable at the pixel level. They share identical WCS geometry and nearly complete overlap in positive-ivar support. Any consistency failures are therefore not at-

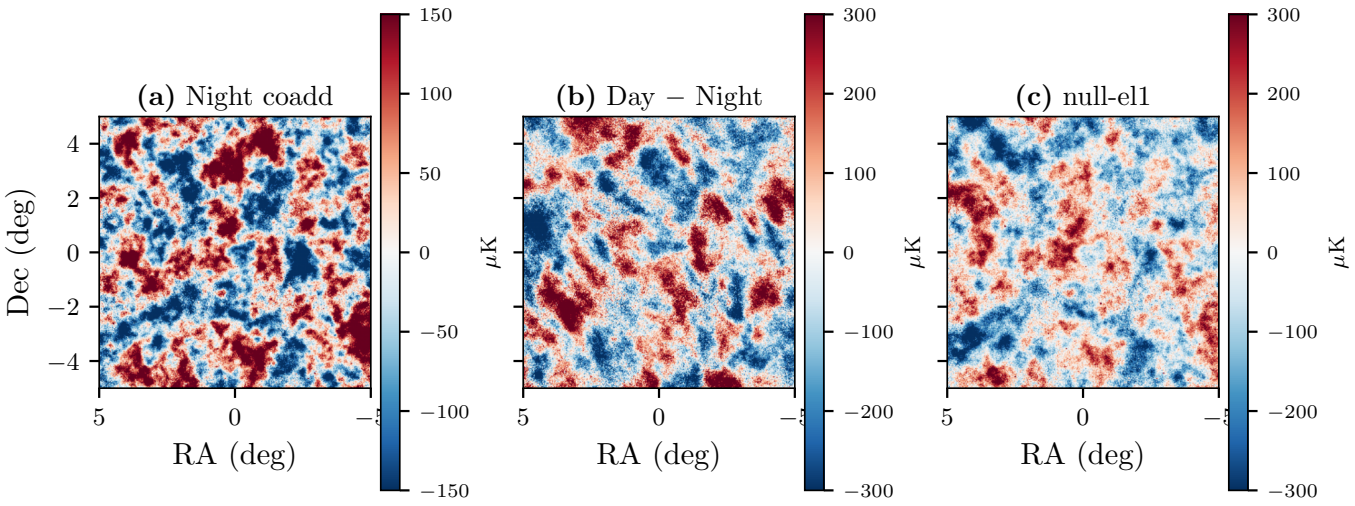

Figure 3. $10^\circ \times 10^\circ$ cutouts of the PA5 f_{090} AA temperature maps centered on the equator. **(a)** Nighttime coadd, showing CMB fluctuations ($\pm 150\ \mu$K color scale). **(b)** Day−night difference ($\pm 300\ \mu$K), revealing large-scale coherent residuals beyond the CMB signal. **(c)** null-el1 map ($\pm 300\ \mu$K), showing rougher, smaller-scale scan-structured residuals qualitatively distinct from the day−night difference.

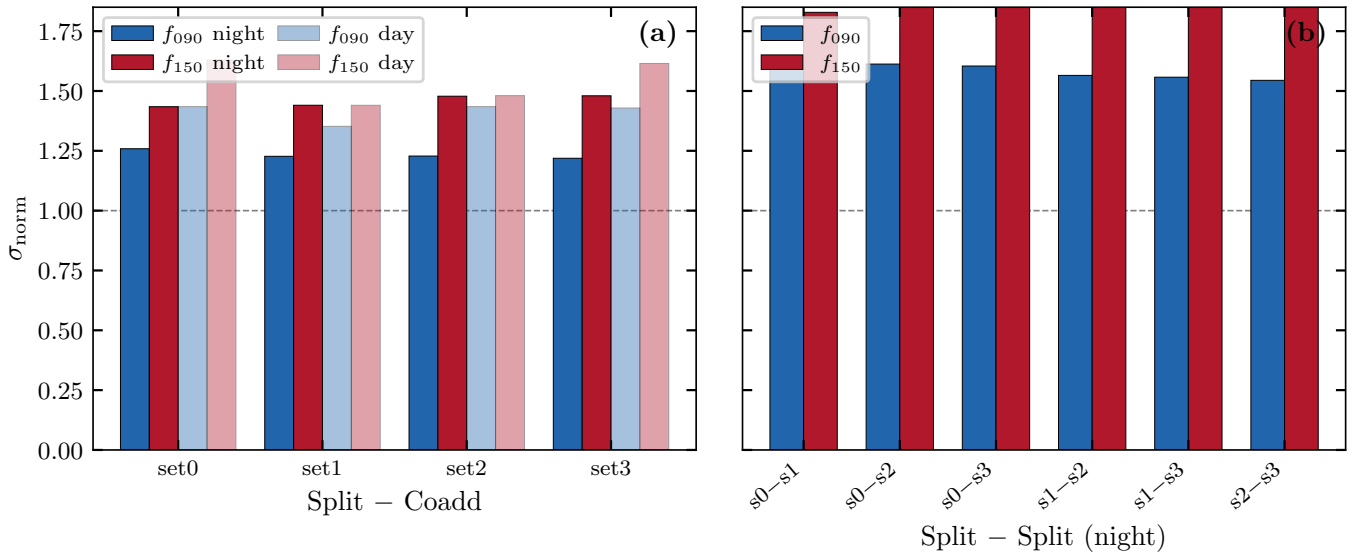

Figure 4. Per-split normalized residual widths for AA maps. **(a)** Set−coadd $\sigma_{\rm norm}$ for each of the four time splits, with nighttime (solid) and daytime (faded) shown separately at both frequencies. **(b)** Pairwise set−set $\sigma_{\rm norm}$ for nighttime data. The dashed line marks $\sigma_{\rm norm} = 1$. The excess is stable across splits and systematically larger at 150 GHz.

tributable to coverage mismatches or coordinate artifacts.

Second, the released inverse-variance weights systematically underpredict the empirical pixel-level scatter between maps. This manifests as $\sigma_{\rm norm} > 1$ across all comparison types—day−night, set−coadd, and set−set—at both 90 and 150 GHz. The excess is larger at 150 GHz ($\sigma_{\rm norm}$ up to 2.02) than at 90 GHz (up to 1.88), suggesting a frequency-dependent component. Possible contributors include: (i) correlated atmospheric noise not captured by the per-pixel white-noise model implicit in the ivar maps, (ii) residual ground pickup or scan-synchronous signals, (iii) thermal dust or other foreground residuals that are stronger at 150 GHz, or (iv) ivar miscalibration that grows with frequency. The small weighted-mean offsets ($\lesssim 1\ \mu$K) indicate that the excess is in variance, not in mean level.

Third, null-el1 maps exhibit a rougher, higher-variance morphology than standard coadds, and this pattern repeats across independent arrays. The gradient-RMS enhancement (×1.67–1.84) being stronger than the variance enhancement (×1.30–1.54)

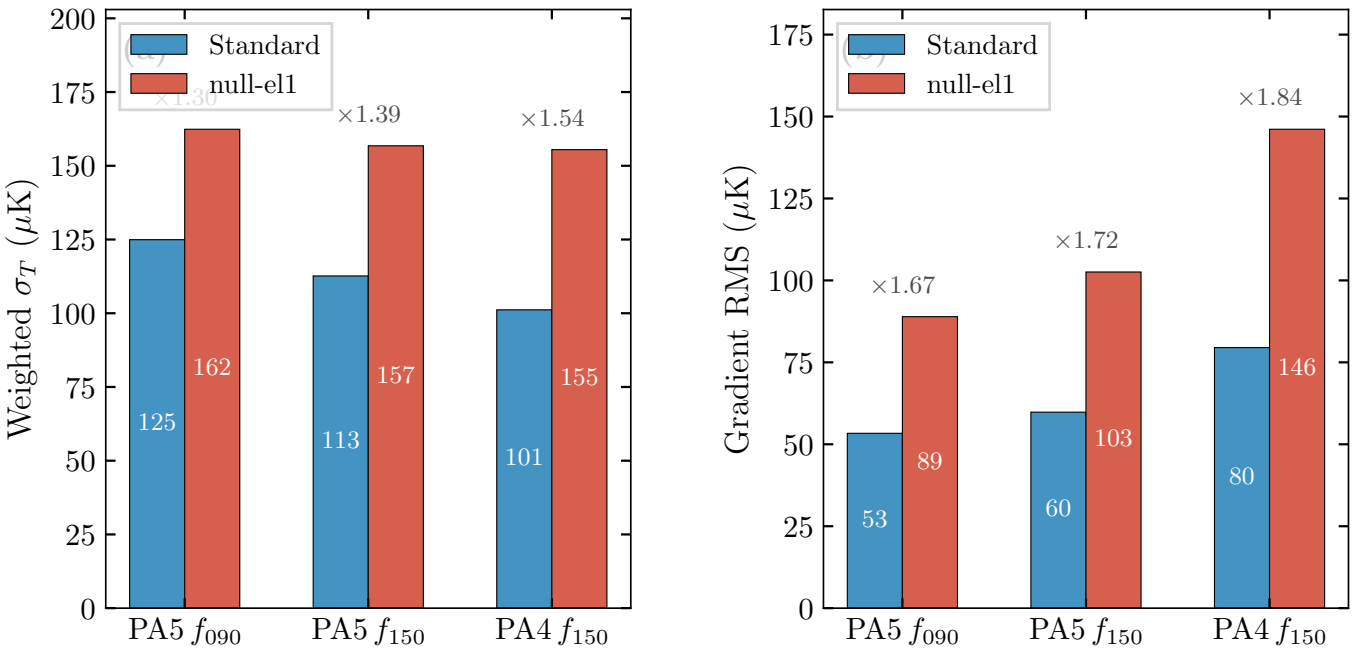

Figure 5. Null-el1 versus standard map statistics in the top-10% ivar core. **(a)** Weighted standard deviation of the temperature field. **(b)** Pixel-scale gradient RMS (roughness proxy). Ratios are shown above each pair. The roughness enhancement (×1.67–1.84) exceeds the variance enhancement, indicating excess power at small angular scales.

points to excess power at small angular scales, consistent with scan-structured residuals dominating the null maps. The visual contrast between the day−night difference (Figure 3b, showing smoother large-scale residuals) and the null-el1 map (Figure 3c, showing rougher small-scale structure) suggests that different systematic contributions dominate these two diagnostics.

These findings do not indicate a failure of the DR6 data products for their intended cosmological applications: the power-spectrum pipeline employs cross-spectra, mode-coupling corrections, and transfer-function modeling that address many of the effects visible in raw map-domain statistics. Rather, they establish quantitative benchmarks for the level of non-ideality present in the released maps, which is useful for any analysis that operates at the map level—component separation, cluster finding, stacking, or lensing reconstruction.

A natural extension of this work is a harmonic-domain analysis using the four-way split cross-spectra with beam harmonization, which would decompose the excess variance into signal, noise, and systematic contributions as a function of multipole ℓ. The daytime beams provided in the DR6 release make it possible to assess how much of the day–night excess is attributable to beam differences versus noise properties. The NILC component-separated maps (Coulton et al. 2024) provide an additional avenue: cross-correlating NILC outputs against single-frequency maps would test whether the excess variance propagates into the foreground-cleaned products.

6. CONCLUSIONS

We have established a reproducible map-domain internal-consistency baseline for ACT DR6 AA temperature maps at 90 and 150 GHz. The key findings are:

- Day and night AA coadds are structurally matched with the expected depth ratios (×1.76–1.77), but ivar-normalized residual widths of $\sigma_{\rm norm} \approx 1.9$–$2.0$ indicate significant excess scatter beyond the released noise model.

- Nighttime split tests yield $\sigma_{\rm norm} \approx 1.2$–$1.9$ across all set−coadd and set−set comparisons, confirming that the excess is a generic property of the maps, not specific to the day–night boundary.

- Null-el1 maps show ∼1.7–1.8× enhanced pixel-scale roughness relative to standard coadds, consistent with scan-structured residuals, and the pattern is stable across two frequencies and an independent detector array.

- The excess is systematically larger at 150 GHz than at 90 GHz, suggesting a frequency-dependent contribution from atmosphere, foregrounds, or ivar calibration.

These results motivate a publication-grade harmonic-space follow-up using split cross-spectra, beam deconvolution, and transfer-function corrections to disentangle noise, systematics, and signal contributions as a function of angular scale.

This analysis was produced by the CosmoEvolve autonomous research lab using publicly available ACT DR6.02 data products. We acknowledge the ACT collaboration for making these data available. This work made use of the `pixell` (Naess et al. 2025), `astropy`, and `numpy` software packages.

REFERENCES

Calabrese, E., et al. 2025, Journal of Cosmology and Astroparticle Physics, 2025, 063, doi: 10.1088/1475-7516/2025/11/063

Coulton, W. R., et al. 2024, Physical Review D, 109, 063530, doi: 10.1103/PhysRevD.109.063530

Louis, T., et al. 2025, Journal of Cosmology and Astroparticle Physics, 2025, 062, doi: 10.1088/1475-7516/2025/11/062

Naess, S., et al. 2025, Journal of Cosmology and Astroparticle Physics, 2025, 061, doi: 10.1088/1475-7516/2025/11/061

Qu, F. J., Sherwin, B. D., Madhavacheril, M. S., et al. 2024, The Astrophysical Journal, 962, 112, doi: 10.3847/1538-4357/acfe06